

# Velocity profile effects on a bottom-mounted square cylinder wake and load variations

Maëlys Magnier, Grégory Germain, Benoît Gaurier, and Philippe Druault

**Abstract**—The development of Marine Renewable Energies leads to install structures in areas with strong and turbulent currents. In this kind of area, the vertical velocity profile is a function of the seabed roughness and of the tidal range, creating various velocity profile shapes. Bottom structures (tidal energy converter, sub-sea substation) are then brought to significant poorly understood wake and load variations. A generic study is thus developed to quantify the impact of vertical velocity profiles on a bottom-mounted obstacle in terms of load variations. This case study is also useful to better understand the energetic wake of a large obstacle in a tidal stream. Four velocity profiles are considered. Three are grid generated velocity profiles homogeneous transversely in the tank and one is the 3D flow generated by an isolated bottom cube. Loads on an aspect ratio cylinder of 6 and flow characteristics are analysed to characterise the impact that the different vertical velocity profiles can have on the behaviour of the cylinder in terms of load and wake evolution. The results show that an isolated roughness has a stronger impact on the bottom structure wake development than the vertical velocity profiles studied here, for which levels of the 1st and 2nd order statistics are slightly modified. The load analysis shows differences between each case, suggesting the strong impact of punctual large vortices.

**Index Terms**—Marine energy; Tidal vertical velocity profiles; Wall-mounted cylinder; PIV; Loads;

## I. INTRODUCTION

WIDE bottom-mounted structures are often encountered in Marine Renewable Energies site. These structures can be human brought as tidal energy converters and subsea hubs [1] or being natural seabed obstacles like large bathymetry variations. These structures being often exposed to a high Reynolds number flow, it is of great significance to investigate the hydrodynamic forces on these structures as well as the wake behaviour. Many experimental studies have been carried out to analyse the effects of high Reynolds flows over surface-mounted structures over decades. Simple geometries of obstacles like wall-mounted square cylinders or dunes are used for these studies. Martinuzzi et al. [2] found that there is, around the symmetry plane, a two-dimensional middle region in the wake, behind the structures with an aspect ratio larger than 6.

The authors would like to thank Jean-Valéry Facq and Thomas Bacchetti for their technical support. This research was partly funded by the European Commission H2020 Programme for Research & Innovation – “RealTide Project”, grant number 727689 and by the Region Hauts-de-France in the framework of the project CPER 2015-2020 MARCO.

P. Druault is at Sorbonne Université, CNRS, Institut Jean Le Rond d’Alembert, FR-75005 Paris, France.

M. Magnier, B. Gaurier and G. Germain are at the French Research Institute for Exploitation of the Sea (IFREMER) Centre Manche—Mer du Nord, Boulogne sur Mer FR-62321, France (e-mail: maelys.magnier@ifremer.fr).

[3], [4] highlighted that Kelvin-Helmholtz vortices are generated periodically from the upstream edge of wide obstacles and they fully interact or merge to create downstream hairpin structures.

All these studies have been made for small vertical extend boundary layers compared to the obstacle height and small turbulent intensity outside the boundary layer. However, owing to friction from the seabed, the current velocity profile has a non-linear shape with velocity vertical gradient that extent in all water column. Tidal currents are also turbulent. These vertical velocity profiles can modify the flow behaviour around the obstacle and thus mitigate conclusions done with a small vertical extend boundary layer. Indeed, Arie et al. [5] studied the flow over wall-mounted rectangular cylinders subjected to turbulent boundary layer flow and concluded that the pressure coefficient on the structure surface is correlated with the thickness of the boundary layer. Moreover, the shape and form of the separation region over and behind the obstacle depends on the relative boundary layer thickness,  $\delta/H$ , as the location of the separation point upstream from the obstacle [2]. This has been confirmed by comparing different boundary layers over 2D bluff bodies, as Akon et al. [6], who shows that turbulence intensity significantly affects reattachment lengths contrary to turbulence integral length scale. Moreover, Wang et al. [7] suggests that the flow around the cantilevered square cylinder forms coherent spanwise vortex shedding regardless of the oncoming flow conditions. But the turbulent boundary layer tends to change the symmetric vortex shedding from the cylinder to the anti-symmetric. Recently, Kozmar [8] found differences in pressure characteristics on wall-mounted cubes when changing the type of structures in atmospheric boundary layers.

As vertical velocity profiles impacted the wake development of wide wall-mounted structures, the present study aims to understand the interaction between a wide structure and tidal-like vertical velocity profiles better. Mean loads and wake development of a square cylinder subjected to different incoming-flows, three vertical velocity profiles and the wake of an isolated roughness, are first studied. Second, the loads and wake fluctuations are studied instantaneously and in terms of frequency content.

## II. EXPERIMENTAL SET UP

### A. Flume tank

Tests are carried out in the wave and current circulating tank of IFREMER located in Boulogne-sur-Mer

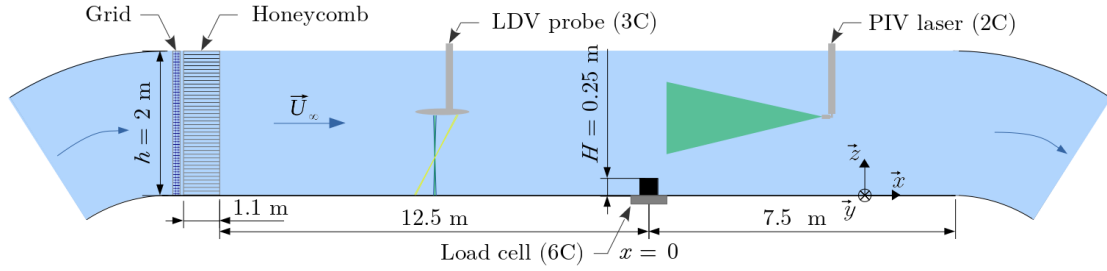


Fig. 1. Schematic view of the wave and current flume tank of Ifremer, with the square cylinder mounted on the load-cell, the PIV laser and the 3C LDV probe.

(France). The test section is 20 m long  $\times$  4 m wide  $\times$  2 m deep (see Fig. 1). The incoming flow ( $U_\infty, V_\infty, W_\infty$ ) is assumed to be steady and constant, with the imposed velocity:  $U_\infty = 1 \text{ m.s}^{-1}$  and  $V_\infty = W_\infty = 0 \text{ m.s}^{-1}$ . The three instantaneous velocity components are denoted ( $U, V, W$ ) along the ( $x, y, z$ ) directions respectively. According to the Reynolds decomposition, each instantaneous velocity component is separated into a mean value and a fluctuating part:  $U = \bar{U} + u'$  where the over-bar indicates the time average.

When the tank is in its original configuration, a low turbulence intensity  $I_\infty = 1.5 \%$  is reached thanks to a grid combined with a honeycomb placed at the inlet of the working section [3] and the boundary layer height, calculated as follows  $\delta_{95} = z (\bar{U} = 0.95 \times U_\infty)$ , is equal to  $\delta_{95} \approx 0.25 \text{ m}$ . During the experiments presented here, the original grid (used to obtain an homogeneous flow with 1.5 % turbulence) is modified to obtain different and more realistic tidal-stream velocity profiles. These new inlet grids are detailed in section II-D2.

### B. Cylinder as large seabed roughness

During this study, the wide seabed obstacle is represented by a square cylinder of section  $H \times H$ , with  $H = 0.25 \text{ m}$ . The cylinder is  $6H$  long, corresponding to an aspect ratio of 6. The  $x$ -origin is set at the centre of the cylinder.  $z = 0$  corresponds to the tank floor. The cylinder is centred in the span-wise direction of the tank. Span-wise origin ( $y = 0$ ) is set to the centre of the cylinder, and thus of the tank (Fig. 1). To estimate loads on the cylinder due to flow, it is attached to a six-components SIXAXES load-cell. The load-cell enables forces until 1500 N and moment until 1000 N.m to be measured and its sampling frequency is set to 128 Hz. The load-cell is fixed on top of the tank floor. The load-cell is inside the cylinder and attached by 12 screws through the top face (PVC, 5 mm thickness) of the cylinder, as presented Fig. 2. The cylinder is raised by 5 mm to avoid touching the tank floor.

For the present investigation, the incoming flow Reynolds number is  $Re_H = \frac{HU_\infty}{\nu} = 2.5 \times 10^5$  with  $\nu$  the water kinematic viscosity. The Froude number is equal to  $Fr = \frac{U_\infty}{\sqrt{g \times h}} = 0.23$ , with  $h$  the flume tank depth and  $g$  the gravity. The scaled experiment has then non-dimensional parameters similar to those of real sea conditions [3], for which the Alderney Race conditions (a potential tidal site in French water) has been considered.

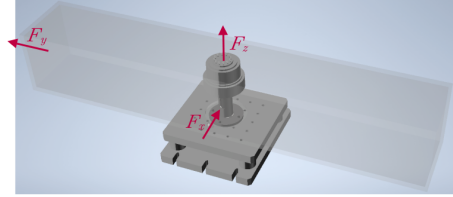


Fig. 2. CAD view of the square cylinder (blurred shape) fixed to the load-cell. The measuring load-cell (of cylindrical shape) is fixed to a metallic structure (square shape) on the floor of the tank. The tank floor is at the level of the top of the metallic structure.

### C. Velocity measurement

To characterize the flow, two means of measurement are used. Before measurements, the tank is seeded with  $10 \mu\text{m}$  diameter silver coated glass micro-particles. A 3 Components Laser Doppler Velocimetry (3C LDV) is used to measure incident velocity profiles. Its sampling frequency depends on the number of particles viewed by the sensor of the probe during the measurement. The LDV acquisition frequency is higher than 100 Hz for the three components of the data used in this study. Particle Image Velocimetry (PIV) measurements are conducted in the symmetry plane of the cylinder, on its top and in its near wake. They are synchronized with load-cell measurements to link velocity and load fluctuations. Particles are illuminated by a 200 mJ Nd-YAG laser and detected by the camera FLOWSSENS EO-2M. Cross-correlation (on  $32 \text{ pix} \times 32 \text{ pix}$  windows) is used to calculate particle displacement between two images ( $1200 \mu\text{s}$  between both) and outliers are replaced with the Universal Outlier Detection method. PIV acquisitions are made during 200 s, hence 3000 double images are taken with a 15 Hz acquisition frequency. Plane dimensions are  $1142 \times 699 \text{ mm}^2$  with a spatial resolution of  $dx = dz = 11.7 \text{ mm}$  (see Fig. 3). The reader can be referred to previous works [3] for details about experimental set-up and the measurement method.

### D. Velocity vertical profiles modelling

During the 5<sup>th</sup> last years, a lot of work has been done to better understand the energetic wake of wall-mounted cylinder for the purpose of Marine Renewable Energies [3], [9]–[11]. Studies have been carried out in the tank in its original configuration: constant velocity along the depth, except in the small boundary layer. However, real tidal velocity profiles

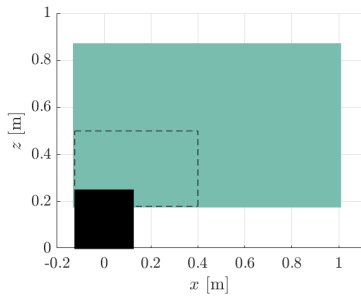


Fig. 3. PIV measurement plane representation. Black: side view of the square cylinder. Green: Entire PIV plane. Dashed rectangle: part of plane showed in Fig. 11.

are more complex.

1) *In-situ current velocity profile*: At sea, the current velocity profile has a non-linear shape. These profiles are multiple depending on the site, the tidal range (spring, neap, in between), the direction of the flow (ebb or flood), and of mete-ocean conditions (swell comes with orbital velocity). One way to define current velocity profiles is to use power laws, enabling us to compare the profiles thanks to a unique coefficient  $\alpha$ .  $U_{PowerLaw}$  is defined as:

$$U_{PowerLaw}(z) = U_{ref} \times \left( \frac{z}{D_e} \right)^{1/\alpha} \quad (1)$$

with  $U_{ref}$  corresponding to the surface velocity (or velocity at mean depth),  $D_e$  represents the depth of the water column and  $z$  the distance from the bottom. Note that some real velocity profile does not fit with this simple law, as current velocity profiles observed at Paimpol-Bréhat [12]. In the Aldernay Race (France), a large study has been made, using towed ADCP [13]. Sea was calm (light wind), waves' effects are thus neglected. They found current velocity profiles with  $\alpha$  included between 4 and 14. However, a trend stands out:  $\alpha = 7$  power law is representative of many Marine Renewable Energies sites [14]–[17].

2) *Reproduction of in-situ profile in the flume tank*: To get closer to real tidal-stream in terms of velocity profile, the flow of the tank has been modified using grid and mesh arrangements. Three inlet flows have been chosen. The first inlet flow is the reference one. It is the original flow of the flume tank (presented in II-A.). It is named "Original grid" in the following. Then, two vertical velocity profiles are generated with two mesh arrangements added to the original grid of the tank. Their detailed composition is presented in Fig. 4. In the following, they are named "Panel 1" and "Panel 2".

To complete this study, the effect of flow generated by an isolated roughness is studied. The particular roughness is a cube of side  $H$ , located  $2H$  upstream from the cylinder (see Fig. 5). Its 3D wake will interact differently with the cylinder.

### III. UPSTREAM FLOWS CHARACTERIZATION

In this section, mean velocity profiles and turbulent intensity are depicted, first for the three vertical velocity profiles coming from meshes arrangement and then

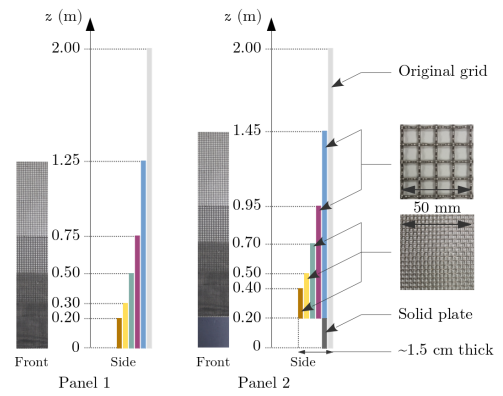


Fig. 4. Grids and meshes arrangement for the generation of specific vertical velocity profile. (Non-uniform in the vertical direction but uniform on the whole width of the tank.) Note that the Panel 2 is simply made of the Panel 1 placed over a 20 cm high solid plate.

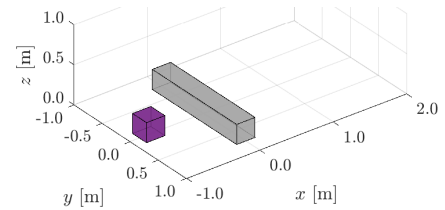


Fig. 5. Isolated obstacle represented as a cube of side  $H$  in the experiment,  $2H$  upstream from the square cylinder. The cube is in purple on the figure.

for the isolated obstacle. Furthermore, mean velocity profiles are compared with two tidal-stream velocity profiles encountered in the English Channel.

#### A. Grid generated vertical velocity profiles characterization

1) *Mean velocity*: Fig. 6 presents mean profiles of the streamwise velocity  $\bar{U}$ , at  $(x, y) = (0 \text{ m}, 0 \text{ m})$ , along  $z$ , the height of the tank. Here, the incoming velocity is set to  $U_\infty = 1 \text{ m.s}^{-1}$ . Measurements have been done for different incoming velocities. Note that, between  $U_\infty = 0.6 \text{ m.s}^{-1}$  and  $U_\infty = 1.2 \text{ m.s}^{-1}$ , the shape of the velocity profile does not depend on the imposed velocity. Also, profiles don't vary with  $x$  and  $y$ . For the three grid combinations, a point corresponds to a 3C LDV measurement point. At each measurement point, the mean velocity  $\bar{U}$  and the standard deviation  $\sigma(U)$  of the streamwise velocity are calculated and plotted as a dot and an error bar. Dashed lines correspond to an interpolated profile of  $\bar{U}$  from these points. These interpolated profiles are the ones use in the following, for future comparative analyses.

In blue in the figure, the mean streamwise velocity profile generated by the Original grid is almost constant along  $z$ , except in its boundary layer that extends until  $z \approx H$ . In this thin boundary layer, a very high velocity gradient is present. Over the rest of the water column ( $z > H$ ), the velocity gradient is close to zero. On contrary,  $\bar{U}$  is growing with  $z$  over almost all water column for Panel 1 and Panel 2. Their mean gradients (over the tank height) are larger than Original grid one because their boundary layers extend upper in the water column. For the Original grid case, the obstacle is immersed in a thin boundary layer. For Panel 1 and

Panel 2 cases, it is completely immersed in a vertical velocity profile that is sheared from the tank floor to the water surface. Moreover, the more the flow slowed in the bottom part of the tank, the more accelerated in the upper part. Comparing each case, the average velocity over the tank height  $h$  is almost the same (Table I). The flow-rate is conserved.

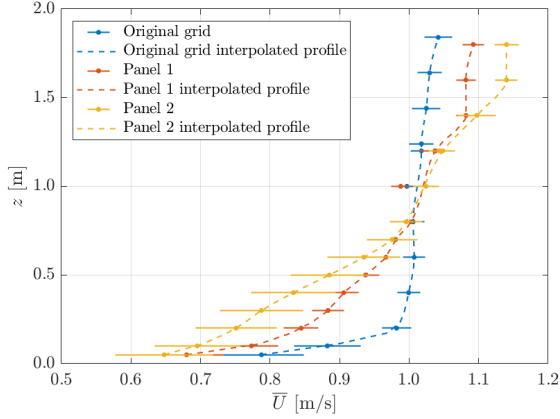


Fig. 6. Dots & errorbars:  $\bar{U} \pm \sigma(U)$  from LDV 3C measurement. Dashed lines, mean velocity profile use for the following.

2) *Turbulent intensity*: Fig. 7 presents the 3D turbulent intensity  $I_\infty$  at  $(x, y) = (0 \text{ m}, 0 \text{ m})$ , in flow coming from the three grid configurations. It is defined as:

$$I_\infty = 100 \frac{\sqrt{\frac{1}{3}(u'^2 + v'^2 + w'^2)}}{\sqrt{U_\infty^2 + V_\infty^2 + W_\infty^2}} \quad (2)$$

As before, between  $U_\infty = 0.6 \text{ m.s}^{-1}$  and  $U_\infty = 1.2 \text{ m.s}^{-1}$ , the turbulent intensity does not depend on the imposed velocity.

Two behaviours appear in this figure. For the Original grid and the Panel 1 cases,  $I_\infty = 1.5\%$  excepted in a small layer (that have the height of the Original grid boundary layer) where it is higher due to the interaction of the floor with the flow. Panel 2 generates a higher turbulent flow in the bottom half of the tank. It reaches  $8\%$  near the ground and  $I_\infty(z = 0.05 : 1) = 5.0\%$  versus  $I_\infty(z = 0.05 : 1) = 2.2\%$  for the Original grid and Panel 1. This difference in turbulence intensity is due to the solid plate in the bottom part of Panel 2 that prevents the flow to go through honeycomb and create backward facing step like condition. This solid plate also modifies pressure gradient and the energy distribution [18].

### B. Isolated roughness flow characterization

To represent an isolated obstacle, a cube of side  $H$  is chosen. It is fixed  $2H$  upstream from the cylinder. Contrary to Panel 1 and Panel 2, the cube generates a 3D flow that makes the interaction cube-cylinder really complex.

Fig. 8 presents streamlines around the cube when it is alone. Data have been measured with PIV and a detailed study can be found in [19]. Along  $y$ -axis, the cube mainly disturbs the flow on  $2H$ , and along  $z$  of  $1.5H$ . Its interaction with the stream creates three recirculation regions (in front, on top, and behind

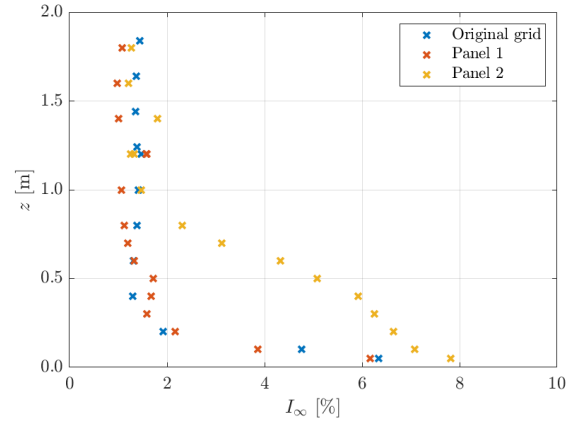


Fig. 7. Turbulent intensity behind each vertical velocity profile whatever the inlet velocity.

it) and is responsible for a horseshoe vortex coming from the recirculation region in front of the body that extends around the sides of the body (see [2], [20]).

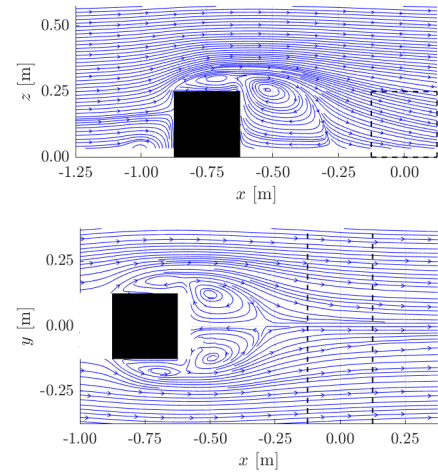


Fig. 8. Mean velocity streamlines. Top:  $y = 0$ . Bottom:  $z = 0.6 \times H = 0.15 \text{ m}$ . Dashed lines show the cylinder position. Data issued from PIV measurement campaign presented in [19].

Fig. 9 presents the mean velocity in two planes perpendicular to the flow, in the wake of the cube. The two planes are positioned  $1H$  and  $2H$  (the cylinder location) behind the cube. The horizontal line is at  $0.6H$  of the floor and the vertical one is at  $y = 0H$ . At  $x = 2H$  downstream of the cube, the cylinder is not in the recirculation zone of the cube. However, the flow which impacts the cylinder is clearly modified.  $\bar{U}$  is not larger than  $0.3 \text{ m.s}^{-1}$  behind the cube and recovers the upstream velocity when  $x > 3H$ .

### C. Comparison with real tidal-stream velocity profiles

To compare in-situ profiles to tank ones, they are normalized by the velocity average on a turbine height. This choice has been made because the next step of this study is to focus on vertical velocity profile effect on a tidal turbine. In-situ, these tidal turbines can be set near the ground on foundations or being fixed on floating structures. In the tank, it is set at half-height. To fit with future tank experiments, the instrumented turbine presented in [21] is chosen to normalize all

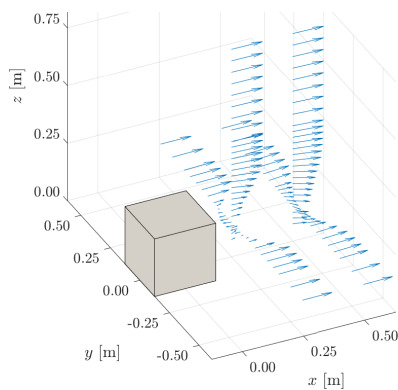


Fig. 9. Representation of the impact of the cube on the mean velocity. Data issued from LDV measurement campaign presented in [19]

quantities. Its diameter  $d_{turbine}$  measures 0.8 m and it extends from  $z = 0.6$  m to  $z = 1.4$  m in the flume tank. The velocity used to normalize the other velocities is thus calculated as:  $\overline{U}_{turbine} = \overline{U}(z^* = 0.3 : 0.7)$  with  $z^* = z/\overline{D_e}$  and  $\overline{D_e}$  the mean depth, at sea as in the tank.

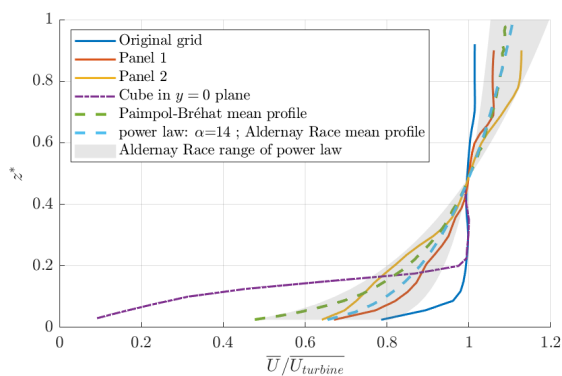


Fig. 10.  $U$  normalized by the velocity averaged between  $z^* = 0.3$  and  $z^* = 0.7$ , the vertical extend of swept area of the turbine model used at Ifremer.  $z^* = z/\overline{D_e}$ , with  $\overline{D_e}$  the mean depth (in the tank,  $\overline{D_e} = h$  and at sea, it corresponds to the average water height on a tidal cycle)

Looking at Fig. 10, the Original grid velocity profile slope is too important to correspond to a real tidal-stream turbine. On contrary, Panel 1 and Panel 2 globally correspond to in-situ mean velocity profile. However, their shapes do not fit perfectly neither with Paimpol-Bréhat [12] nor with Aldernay Race [14] velocity profiles, but they stay in Aldernay Race range of profiles. They are thus comparable with in-situ profiles in terms of velocity and will be used to study the impact of shear profiles on the near-wake development of the cylinder. Note that the impact of the in-situ turbulent intensity level is not studied here and can mitigate our results, as the level of turbulence is higher in-situ than in tanks [22]. Moreover, cube central plane mean streamwise velocity profile distinguishes from grid and in-situ velocity profiles by its extremely large velocity gradient under  $z^* \approx 0.2$ . It means that the impact of a nearby isolated obstacle differs from tidal velocity profile ones.

#### IV. LOADS AND WAKE MEAN BEHAVIOUR

To characterize the impact of such flows on a wall-mounted structure and to better understand the wake generation, the focus is made on first-order and second-order moment. Mean flow and its fluctuations are studied first. Then loading on the cylinder are investigated.

##### A. Upstream velocity variations effects on the near-wake

Fig. 11 presents mean streamwise velocity  $\overline{U}$ , mean vertical velocity  $\overline{W}$ , 2D turbulent kinetic energy  $k = \frac{1}{2}(\overline{u'^2} + \overline{w'^2})$  and Reynolds stress  $\tau_{uw} = \overline{u'w'}$ , in the near-wake of the cylinder. Those data are a zoom of the measurement planes as showed in Fig. 3. These quantities are presented for the four upstream flows conditions.

Looking at the mean velocities as to  $k$  and  $\tau_{uw}$ , the spatial development of the wake is comparable for the three vertical velocity profiles (Original grid, Panel 1 and Panel 2). However, their levels are reduced due to the reduction of the local velocity inherent to the creation of vertical velocity profiles (see Table I). This is consolidated by Fig. 12, which shows  $\overline{U}$  at four fixed  $x$ . All variations appear at the same height  $z$ . Thus the differences observed on incoming velocity profiles and turbulent intensity (Section III) do not impact the wake dynamic but only its energy.

On contrary, the isolated obstacle has a strong impact on the cylinder near-wake construction.  $\overline{U}$  is globally lower and the recirculation bubble ( $\overline{U} \leq 0$ ) is significantly reduced.  $\overline{W}$  is higher than without the cube on top of the cylinder and negative behind in almost all water column (the part showed here). A lot of turbulent kinetic energy  $k$  is produced on top of the cylinder and globally its level is high on the whole plane presented here. Finally, two shear layers appear instead of one, materialized by a negative  $\tau_{uw}$ . The 3D flow coming from the cube modifies totally the wake of the cylinder. A more detailed study of the impact of the cube on a wall-mounted cylinder can be found in [23].

TABLE I  
AVERAGE VELOCITIES OVER HEIGHT AT  $U_\infty = 1.0$  M/S.

Case	Original grid	Panel 1	Panel 2
$\overline{U}$ over $h$	1.00	0.98	0.97
$\overline{U}$ over $H$ ( $\overline{U_H}$ )	0.92	0.80	0.72

##### B. Focus on local flow conditions

To understand why grids impact the energy of the cylinder near-wake but not its wake dynamic, the focus is done on the incoming velocity viewed by the cylinder. Fig. 13 presents the velocity profiles coming from the Original Grid, Panel 1 and Panel 2 normalized by their respective mean velocity on the cylinder height (the gray region in the figure) presented Table I. Please note that these velocities have been measured without the cylinder, at its position, implying that this is not the exact velocity viewed by the cylinder as its presence locally modifies the flow.

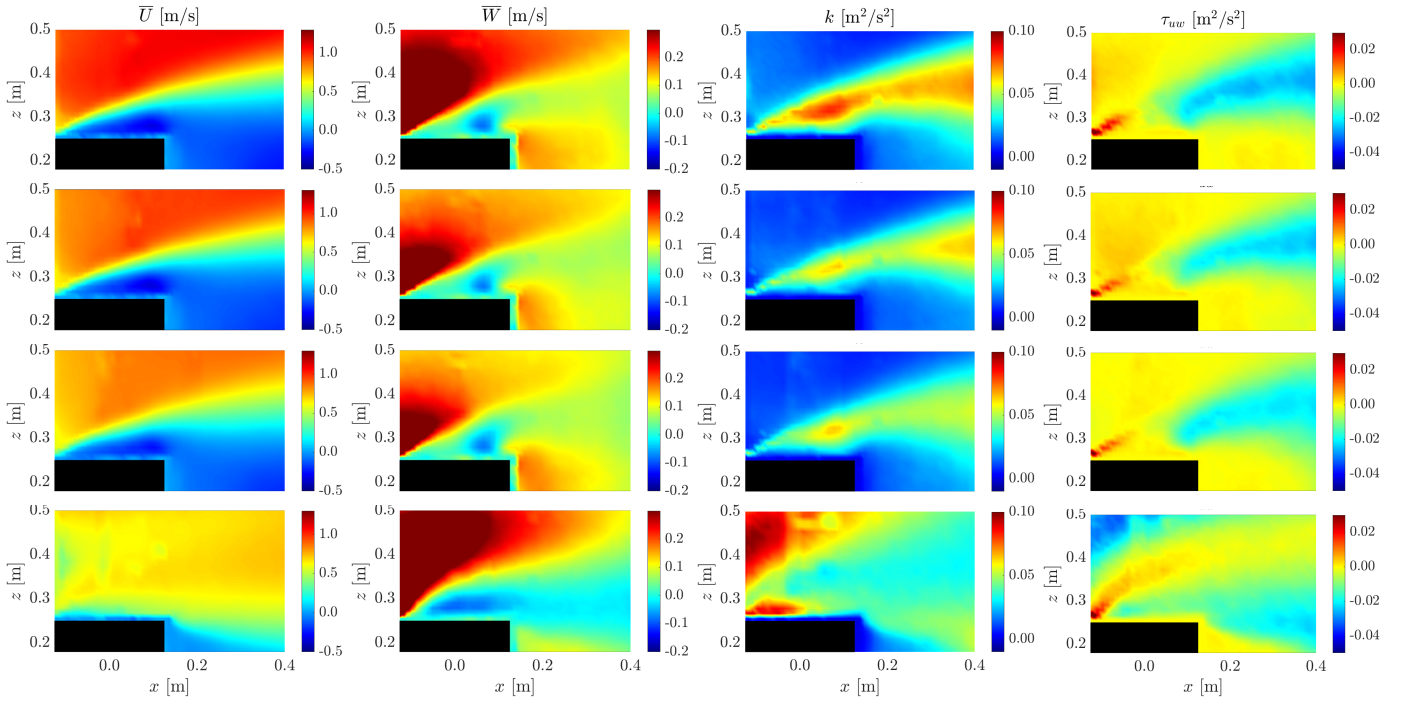


Fig. 11. Averaged map of  $\bar{U}$ ,  $\bar{W}$ ,  $k$  and  $\tau_{uw}$ , from left to right. From top to bottom : Original grid, Panel 1, Panel 2, cube.

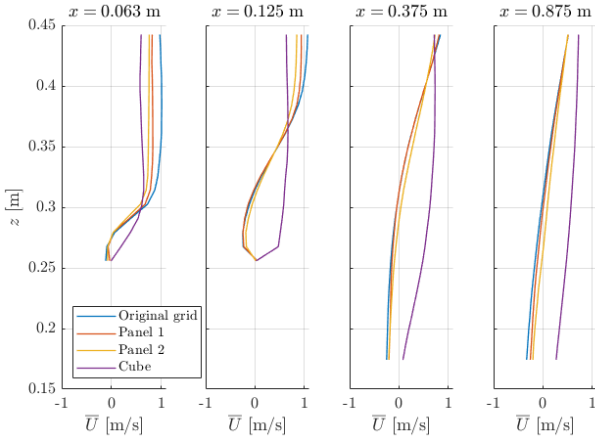


Fig. 12. Mean streamwise velocity profiles as a function of  $z$  in four different streamwise positions.

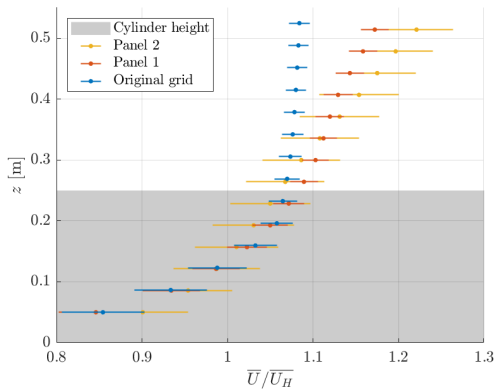


Fig. 13.  $\bar{U}$  normalized by their spatial average over respective cylinder height  $\bar{U}_H$ . Errorbars correspond to the standard deviation of  $U(t)$ . Same data that presented Fig. 6

First, looking at the mean velocity, Original grid and Panel 1 generate the same velocity gradient over

the cylinder height  $H$ . Upper than  $H$ , their slopes start diverging, Panel 1 retaining its gradient while the Original grid velocity profile gradient becomes smaller. Panel 2 has a slightly larger velocity gradient, which remains the same throughout the water column. Then, looking at fluctuations, Panel 2 stands out from the two others boundary layers. Its fluctuations are higher, that corresponds to the higher turbulence intensity observed in Fig. 7.

### C. Loads study

To study the effect of imposed velocity on loads, they have been measured for 6 incoming velocities between  $U_\infty = 0.2 \text{ m.s}^{-1}$  and  $U_\infty = 1.2 \text{ m.s}^{-1}$  for each flow case. Fig. 14 presents  $\bar{F}_x \pm \sigma(F_x)$  and  $\bar{F}_z \pm \sigma(F_z)$ , with  $\sigma(F)$  the standard deviation of  $F$ . They are the only loads presented here because  $F_y$ ,  $M_x$ , and  $M_z$  are not modified by the interaction flow-cylinder and  $M_y$  is resulting of  $F_x$  so it is evolving the same way. Load orientations are detailed Fig. 2.

For all upstream flows, loads increase when imposed velocity increases, with a typical  $U^2$  behaviour. Mean loads towards  $x$ -direction ( $\bar{F}_x$ ) are larger than towards  $z$ -direction ( $\bar{F}_z$ ). It means that the pressure on the cylinder frontal face grows faster than it decreases on the cylinder top face. Load fluctuations also grow when the velocity increases.

Comparing all cases, the Original grid, at an imposed velocity, is responsible for the maximum load on the frontal face ( $\bar{F}_x$ ). This is due to its small vertical extent boundary layer causing the higher incoming velocity over cylinder height  $H$  (see Table I). It is followed by the cube case, which strongly slows the flow but on the central third of the cylinder length only. Then, it is followed by Panel 1 and Panel 2 respectively, as Panel 2 is responsible for the minimum incoming velocity.

$F_z$  behaviour is more complex. The higher it is, the lower is the pressure force on the cylinder top face. This pressure reduction is linked to the velocity around the cylinder. Panel 1 and 2 cause the same  $\overline{F_z}$ , the lower one. The Original grid is responsible for larger load  $F_z$  thanks to the larger incoming velocity, creating a larger upward directed flow on top of the cylinder. Cube causes the maximum  $F_z$ . Its complex 3D flow relaxes a lot of pressure on the top face of the cylinder.

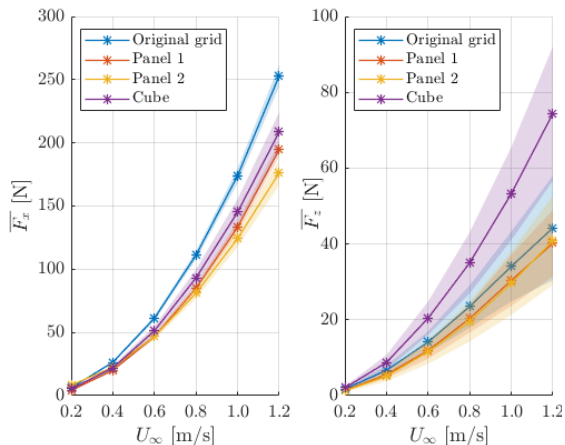


Fig. 14. Mean and standard deviation loads versus the imposed velocity. Left:  $\overline{F_x}$ . Right:  $\overline{F_z}$ . Note that the vertical axis range differs between charts.

To better understand how loads fluctuate, Fig. 15 presents load relative standard deviation in percentage values. For the four inlet conditions,  $\sigma(F_x)/\overline{F_x}$  is constant. Fluctuations are representing less than 10% of the mean load  $F_x$ . The cube 3D flow is the one responsible for the higher variations. Then, Panel 2 generates  $\sigma(F_x)/\overline{F_x} \approx 5\%$ . The Original grid and the Panel 1 have the same relative fluctuations, of approximately 4%.

$F_z$  relative standard deviation is almost 4 times higher than the one observed for  $F_x$  and its behaviour is more complex. It is maximum for the Panel 2 and reaches  $\approx 27\%$ .  $F_z$  relative standard deviation is constant, downstream the cube and the Panel 2 whereas it increases as  $U_\infty$  increases for the Original grid and Panel 1. This difference comes from the turbulent content of the incoming flow that is already present at small velocity for Panel 2 and cube cases. This behaviour suggests differences in flow establishment around the cylinder even is nothing is visible looking at flow first and second-order statistics.

From the following parts, three points stand out:

- When the local incoming velocity  $\overline{U_H}$  is smaller, it reduces  $\overline{U}$ ,  $\overline{W}$ ,  $k$ , and  $\tau_{uw}$ . However, it does not modify the spatial extension of the near-wake on average. Near-wake loses energy but its dynamic is conserved. No conclusion on the whole wake can be emitted because it viewed accelerated velocity in the upper half of the tank that can modify its development.
- The level of turbulence of the incoming flow does not seem to impact the near-wake spatially on average. However, it impacts the loads so the wake is modified even if it is no visible on average.

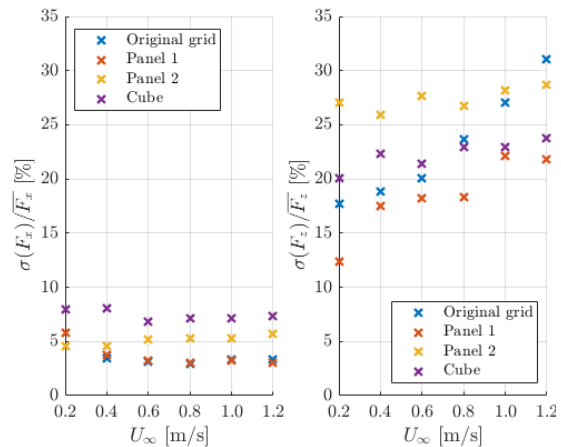


Fig. 15. Relative standard deviation function of the imposed velocity. Left: for  $F_x$ . Right: for  $F_z$

- Load fluctuations are more important along  $z$ -axis and their behaviour is strongly impacted by the turbulence.

## V. IDENTIFICATION OF LOADS AND WAKE FLUCTUATIONS

In this part, the loads and the near wake are studied instantaneously, then their spectral content is studied. The goal is to understand more precisely the wake generation of the cylinder and thus the load behaviour.

### A. Instantaneous study

For the three vertical velocity profile cases, when the comparison is made on loads generated on the cylinder, differences appear on mean and fluctuations. Not only the mean value is slightly reduced due to the local velocity reduction, but the behaviour is modified. On contrary,  $\overline{U}$ ,  $\overline{W}$ ,  $k$  and  $\tau_{uw}$  decrease with the local velocity reduction but the spatial development of the near-wake seems to stay the same. This is contradictory and suggests that flow interactions are complex. To understand this behaviour, one goes back to the analysis of temporal signals.

Fig. 16 presents instantaneous loads  $F_x(t)$  and  $F_z(t)$  between  $t = 0$  s and  $t = 80$  s at an imposed velocity of  $U_\infty = 1.0$  m.s<sup>-1</sup> behind the Panel 1. Both signals fluctuate around their mean value ( $\overline{F_x} = 132$  N and  $\overline{F_z} = 30$  N, plotted in dotted lines in Fig. 16). To study the link between flow and loads viewed by the cylinder, the focus is made on two precise instants (highlighted by dashed lines in Fig. 16). The first one is  $t = 26.3$  s and is chosen at an instant that seems to represent what happens most of the time. The second instant,  $t = 51.6$  s, is chosen at a time where a special event seems to occur. At  $t = 51.6$  s,  $F_x$  reaches its minimum and  $F_z$  reaches its maximum.

At these two times, the instantaneous velocity is represented (see Fig. 17). Velocity patterns are really different. At  $t = 26.3$  s, small vortices appear in the shear layer region, between the outer steady region and the recirculation region. Velocity fluctuations happen but are relatively small. Vortices start developing at the upstream edge of the cylinder and reach  $z = 0.4$  m

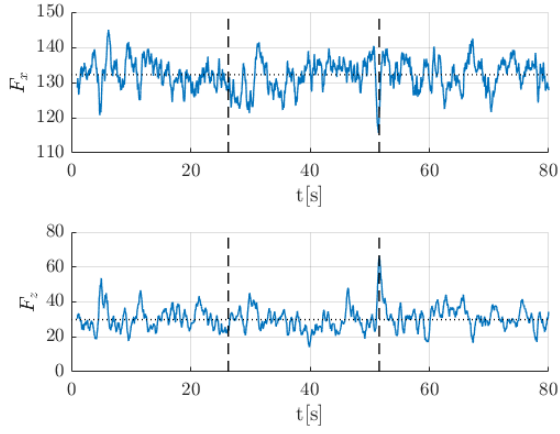


Fig. 16. Instantaneous loads behind Panel 1. Top:  $F_x(t)$ . Bottom:  $F_z(t)$ . Dashed lines are plotted at  $t = 26.3$  s and  $t = 51.6$  s, the times corresponding to the velocity fields plotted on Fig. 17. Dotted lines correspond to mean load  $\bar{F}$ .

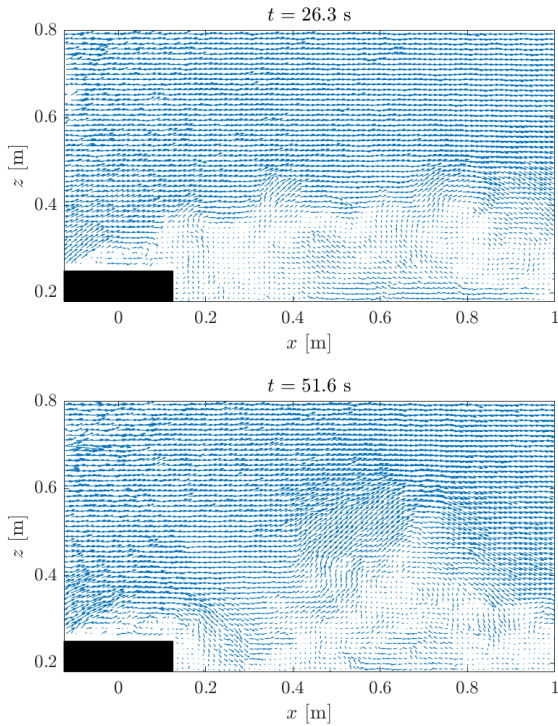


Fig. 17. Instantaneous velocity fields behind Panel 1. Top: at  $t = 26.3$  s. Bottom: at  $t = 51.6$  s.

at  $x = 1$  m. The pattern observed at  $t = 26.3$  s is commonly observed behind the Panel 1, and also behind the Original grid and the Panel 2 (see Fig. 19 and Fig. 21 respectively).

At  $t = 51.6$  s, a specific velocity pattern appears. Instead of having small vortices along the shear layer, two large vortices develop at two distinct heights. A large vortex is in development around the cylinder. This vortex arising pulls the cylinder up with the creation of a maximum on  $F_z$  loads. It seems that this arising structure is coming from the interaction with another large structure centred around  $(x, z) = (0.6 \text{ m}, 0.4 \text{ m})$  and explains why  $F_x$  reaches a local minimum. A deeper study is needed to go further with these interactions. The same kind of structures has been found almost each time that a large peak

can be observed on  $F_x(t)$  (a minimum) and  $F_z(t)$  (a maximum). This conclusion can be extended to the Original grid and Panel 2. Their instantaneous velocity fields and the corresponding instantaneous loads along  $x$  and  $z$  are presented Fig. 19 and Fig. 18 for the Original grid and Fig. 21 and Fig. 20 for Panel 2.

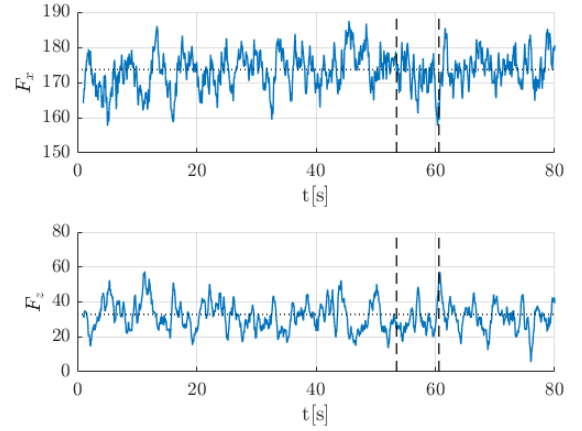


Fig. 18. Instantaneous loads behind the Original grid. Top:  $F_x(t)$ . Bottom:  $F_z(t)$ . Dashed lines are plotted at  $t = 53.5$  s and  $t = 60.6$  s, corresponding to the velocity fields plotted on Fig. 19. Dotted lines correspond to mean load  $\bar{F}$ .

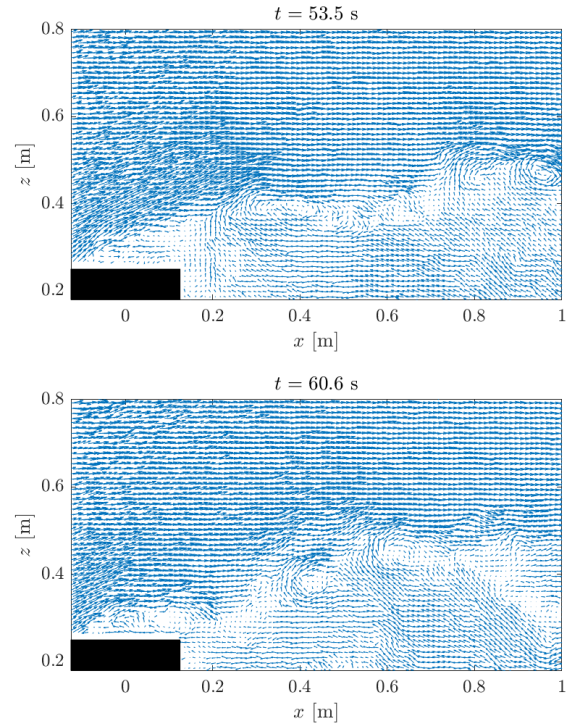


Fig. 19. Instantaneous velocity fields behind the Original Grid. Top: at  $t = 53.5$  s. Bottom: at  $t = 60.6$  s.

Thanks to the study of the instantaneous loads, it puts in evidence two flow regimes downstream the cylinder. The first one consists of small vortices shed in the shear layer region. This flow regime seems to be present most of the time in the flow and has a spatial behaviour that is near the mean flow ones. The second flow regime is when the interaction of the flow with the cylinder creates two large and energetic structures which develop higher in the water column. It seems to occur more punctually.

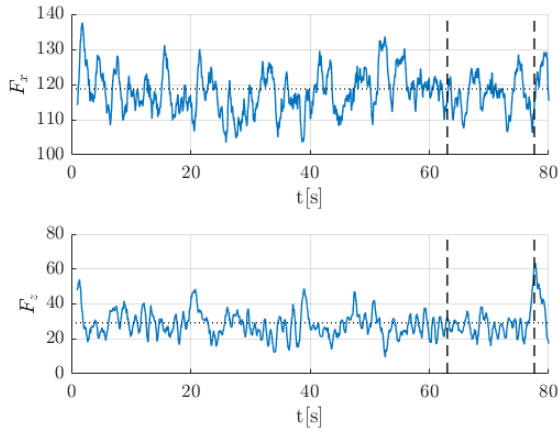


Fig. 20. Instantaneous loads behind Panel 2. Top:  $F_x(t)$ . Bottom:  $F_z(t)$ . Dashed lines are plotted at  $t = 63.0$  s and  $t = 77.6$  s, corresponding to the velocity fields plotted on Fig. 21. Dotted lines correspond to mean load  $\bar{F}$ .

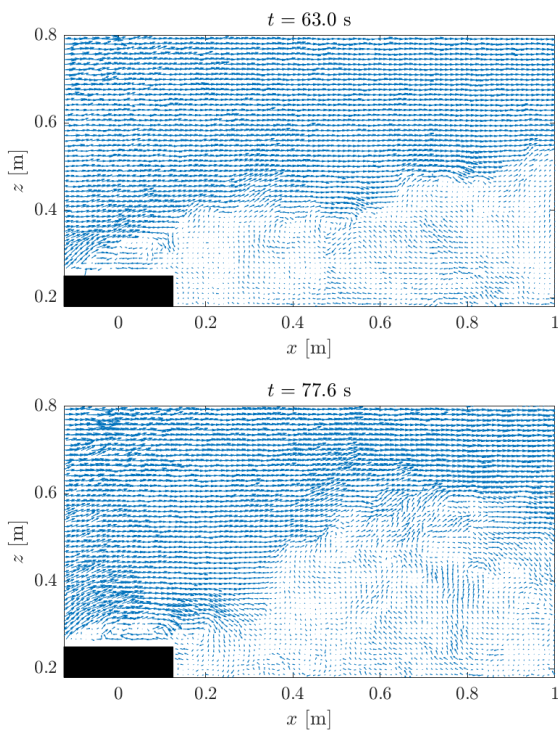


Fig. 21. Instantaneous velocity fields behind the Panel 2. Top: at  $t = 63.0$  s. Bottom: at  $t = 77.6$  s.

If the same pattern appears in each case, they are slightly different between each case. In the first flow regime, vortices are smaller behind the Original Grid and Panel 2 than behind Panel 1. Note that if the height of the shear layer seems to move between case, on average they are superimposed.

These two flow regimes make the cylinder wake complex to understand only with first and second moment analysis. POD or wavelet methods have to be used to extract respectively energetic and rare structures.

### B. Spectral analysis

To complete the instantaneous analysis, the spectral content of  $F_z$  and  $u'$  is studied. Fig. 22 presents  $F_z$  Fast Fourier Transform (FFT). It puts in evidence the

difference of behaviour of Panel 2 compared to the two other boundary layers. Three frequency peaks appear on Original grid FFT, at  $f = 0.2, 0.4$  and  $1.0$  Hz. Two frequency peaks are present in Panel 1 case:  $f = 0.2$  and  $0.4$  Hz. It thus seems that the velocity reduction inherent to Panel 1 decreases the range of frequency where periodical vortices are emitted. On the other hand, Panel 2  $F_z$  spectrum presents a large number of peaks of small amplitude. Instead of having a main range of structure emission, shedding frequencies are scattered and their level is reduced. The turbulence generated by Panel 2 seems to destructure the wake even if it is not visible on mean quantities.

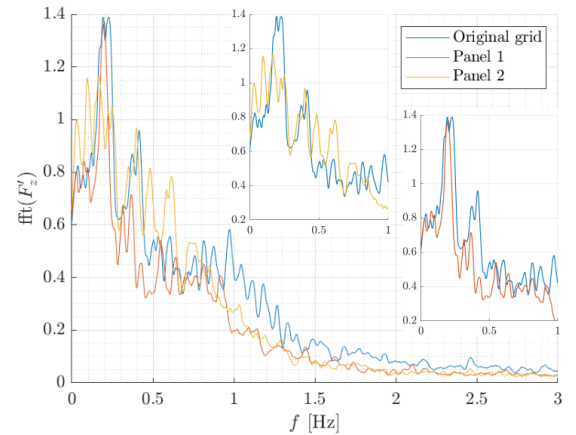


Fig. 22. Fast Fourier Transform of  $F_z$  of the three grid cases only. Two zoom are presented with a Panel compared to the Original grid.

Looking at the fluctuating streamwise velocity Power Spectral Density  $u'$  (Fig. 23), the same conclusions emerge on the effect of the three grid velocity profiles. Original grid wake is the most energetic one and creates regularly, approximately every 5 s, large structures as shown Fig. 19 (bottom). This periodical generation is also present in Panel 1 and Panel 2 but it concentrates less energy. This is due to the velocity decrease inherent to the generation of velocity gradient, and from the turbulence generated by Panel 2. Also, for the three cases, PSD slope is  $-5/3$  slope, confirming the typical dissipation process of turbulence.

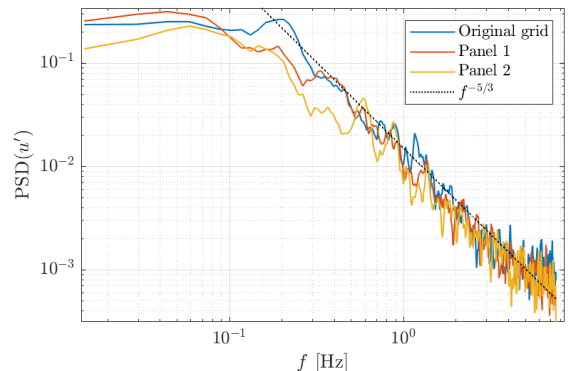


Fig. 23. Power Spectral Density of  $u'$  at  $x = 0.79$  m and  $z = 0.35$  m for the three grid generated velocity profiles.

## VI. CONCLUSION

The objective of the paper is to examine the effects of grid-generated vertical velocity profiles and of an

isolated roughness velocity profile on the development of the wake of a wide bottom-mounted obstacle, represented by a square cylinder of aspect ratio 6. PIV measurements are done in synchronisation with the load measurements, in the wake of the cylinder for the four case studies.

The results show that the grid generated vertical velocity profile does not modify, on average, the spatial development of the cylinder wake. Levels of average velocity and Reynolds' stresses are slightly reduced by the local reduction of velocity inherent to the boundary layers generated by Panel 1 and 2 but the wake dynamic is conserved. The isolated obstacle, on contrary, modifies totally the wake dynamic. The cube wake is thrown up by the cylinder presence avoiding the cylinder wake to develop toward the surface. Two shear layers develop. The repartition of kinetic energy is altered and reaches an especially high level on top and before the cylinder. If the grid-generated velocity profiles do not modify flow first and second moments, loads are impacted by incoming flow turbulence, local velocity and velocity gradient. Their mean values are modified and their fluctuations attest of a modification of the wake dynamic even it is hidden in flow first-order and second-order statistics.

The analysis of instantaneous velocity field confirms the cylinder near-wake differences caused by boundary layer flows. Helped by instantaneous loads analysis, two regimes of vortex shedding are identified, one shedding small structures and the other one shedding large structures linked to strong cylinder loads and occurring at  $f = 0.2$  Hz.

To sum up, the following conclusions can be drawn from the results:

- Grid generated vertical velocity profiles are responsible for different loads on the cylinder. These differences are caused at least by the local velocity and by incoming flow turbulence but a more detailed study is needed to conclude more precisely.
- Grid generated vertical velocity profiles do not modify the near wake dynamic but reduce locally the flow energy due to the local velocity reduction. On contrary, the isolated roughness totally modifies the wake dynamic of the cylinder.
- Two vortex shedding regimes are identified, one occurring most of the time and generating small vortices, the other occurring at a specific frequency and creating large vortices that strongly impact cylinder loads.

## REFERENCES

- [1] N. Hopley and SteveH, "Innovation in Tidal Energy - The Subsea Hub," 2020. [Online]. Available: <https://simecatlantia.com/2020/11/19/innovation-in-tidal-energy-the-subsea-hub/>
- [2] R. Martinuzzi and C. Tropea, "The flow around surface-mounted, prismatic obstacles placed in a fully developed channel flow," *Journal of Fluids Engineering, Transactions of the ASME*, 1993.
- [3] M. Ikhennicheu, G. Germain, P. Druault, and B. Gaurier, "Experimental study of coherent flow structures past a wall-mounted square cylinder," *Ocean Engineering journal*, vol. 182, pp. 137–146, 2019.
- [4] M. Omidyeganeh and U. Piomelli, "Large-eddy simulation of two-dimensional dunes in a steady, unidirectional flow," *Journal of Turbulence*, vol. 5248, 2011.
- [5] M. Arie, M. Kiya, H. Tamura, and Y. Kanayama, "Flow over Rectangular Cylinders Immersed in a Turbulent Boundary Layer. Part 1, Correlation between Pressure Drag and Boundary-Layer Characteristics," *JSME*, vol. 18, no. 125, pp. 532–526, 1975.
- [6] A. F. Akon and G. A. Kopp, "Mean pressure distributions and reattachment lengths for roof-separation bubbles on low-rise buildings," *Jnl. of Wind Engineering and Industrial Aerodynamics*, vol. 155, pp. 115–125, 2016.
- [7] H. Wang, X. Zhao, X. He, and Y. Zhou, "Effects of oncoming flow conditions on the aerodynamic forces on a cantilevered square cylinder," *Journal of Fluids and Structures*, vol. 75, pp. 140–157, 2017.
- [8] H. Kozmar, "Flow, turbulence and surface pressure on a wall-mounted cube in turbulent boundary layers," *Journal of Wind Engineering and Industrial Aerodynamics*, vol. 210, no. December 2020, p. 104503, 2021.
- [9] M. Ikhennicheu, P. Druault, B. Gaurier, and G. Germain, "Turbulent kinetic energy budget in a wall-mounted cylinder wake using PIV measurements," *Ocean Engineering*, vol. 210, no. November 2019, p. 107582, 2020.
- [10] P. Mercier, M. Ikhennicheu, S. Guillou, G. Germain, E. Poizot, M. Grondeau, J. Thiébot, and P. Druault, "The merging of Kelvin–Helmholtz vortices into large coherent flow structures in a high Reynolds number flow past a wall-mounted square cylinder," *Ocean Engineering*, vol. 204, p. 107274, may 2020.
- [11] M. Magnier, P. Druault, B. Gaurier, and G. Germain, "Comparison of bathymetry variation effects on tidal turbine behaviour," in *17ème journées de l'hydrodynamique JH2020*, 2020, pp. 1–12. [Online]. Available: <https://archimer.ifremer.fr/doc/00660/77243/78695.pdf>
- [12] M. Moreau, G. Germain, G. Maurice, A. Richard, and R. Coquet, "HydroQuest : Feedback from Paimpol-Bréhat and validation of the design method," in *Ewtec*, 2021, pp. 1–8.
- [13] A. Sentchev, T. D. Nguyen, L. Furgerot, and P. Bailly du Bois, "Underway velocity measurements in the Alderney Race: towards a three-dimensional representation of tidal motions," *Philosophical transactions. Series A, Mathematical, physical, and engineering sciences*, vol. 378, no. 2178, p. 20190491, 2020.
- [14] L. Furgerot, P. B. Du Bois, Y. Méar, M. Morillon, E. Poizot, and A. C. Bennis, "Velocity profile variability at a tidal-stream energy site (Alderney Race, France): From short (second) to yearly time scales," *2018 OCEANS - MTS/IEEE Kobe Techno-Oceans, OCEANS - Kobe 2018*, pp. 1–8, 2018.
- [15] S. Gooch, J. Thomson, B. Polagye, and D. Meggitt, "Site characterization for tidal power," *MTS/IEEE Biloxi - Marine Technology for Our Future: Global and Local Challenges, OCEANS 2009*, 2009.
- [16] M. Thiébaud and A. Sentchev, "Asymmetry of tidal currents off the W.Brittany coast and assessment of tidal energy resource around the Ushant Island," *Renewable Energy*, vol. 105, pp. 735–747, 2017.
- [17] M. Lewis, S. P. Neill, P. Robins, M. R. Hashemi, and S. Ward, "Characteristics of the velocity profile at tidal-stream energy sites," *Renewable Energy*, vol. 114, pp. 258–272, 2017.
- [18] A. Güemes, C. Sanmiguel Vila, R. Örlü, R. Vinuesa, P. Schlatter, A. Ianiro, and S. Discetti, "Flow organization in the wake of a rib in a turbulent boundary layer with pressure gradient," *Experimental Thermal and Fluid Science*, vol. 108, no. February, pp. 115–124, 2019.
- [19] M. Ikhennicheu, B. Gaurier, P. Druault, and G. Germain, "Experimental analysis of the floor inclination effect on the turbulent wake developing behind a wall mounted cube," *European Journal of Mechanics, B/Fluids*, vol. 72, pp. 340–352, 2018.
- [20] I. P. Castro and A. G. Robins, "The flow around a surface-mounted cube in uniform and turbulent streams," *Journal of Fluid Mechanics*, vol. 79, no. 2, pp. 307–335, 1977.
- [21] B. Gaurier, S. E. Ordonez-Sanchez, J.-V. Facq, G. Germain, C. M. Johnstone, R. Martinez, F. Salvatore, I. Santic, T. Davey, C. Old, and B. G. Sellar, "MaRINET2 tidal energy round robin tests-performance comparison of a horizontal axis turbine subjected to combined wave and current conditions," *Journal of Marine Science and Engineering*, vol. 8, no. 6, 2020.
- [22] I. A. Milne, R. N. Sharma, R. G. Flay, and S. Bickerton, "Characteristics of the turbulence in the flow at a tidal stream power site," *Philosophical Transactions of the Royal Society A: Mathematical, Physical and Engineering Sciences*, vol. 371, no. 1985, 2013.
- [23] M. Magnier, P. Druault, and G. Germain, "Experimental investigation of upstream cube effects on the wake of a wall-mounted cylinder: Wake rising reduction, TKE budget and flow organization," *European Journal of Mechanics, B/Fluids*, vol. 87, pp. 92–102, 2021.